

OPEN

Assessment of the human bone lacuno-canalicular network at the nanoscale and impact of spatial resolution

Boliang Yu¹, Alexandra Pacureanu², Cécile Olivier^{1,2}, Peter Cloetens² & Françoise Peyrin^{1,2*}

Recently, increasing attention has been given to the study of osteocytes, the cells that are thought to play an important role in bone remodeling and in the mechanisms of bone fragility. The interconnected osteocyte system is deeply embedded inside the mineralized bone matrix and lies within a closely fitted porosity known as the lacuno-canalicular network. However, quantitative data on human samples remain scarce, mostly measured in 2D, and there are gaps to be filled in terms of spatial resolution. In this work, we present data on femoral samples from female donors imaged with isotropic 3D spatial resolution by magnified X-ray phase nano computerized-tomography. We report quantitative results on the 3D structure of canaliculi in human femoral bone imaged with a voxel size of 30 nm. We found that the lacuno-canalicular porosity occupies on average 1.45% of the total tissue volume, the ratio of the canalicular versus lacunar porosity is about 37.7%, and the primary number of canaliculi stemming from each lacuna is 79 on average. The examination of this number at different distances from the surface of the lacunae demonstrates branching in the canaliculi network. We analyzed the impact of spatial resolution on quantification by comparing parameters extracted from the same samples imaged with 120 nm and 30 nm voxel sizes. To avoid any bias related to the analysis region, the volumes at 120 nm and 30 nm were registered and cropped to the same field of view. Our results show that the measurements at 120 and 30 nm are strongly correlated in our data set but that the highest spatial resolution provides more accurate information on the canaliculi network and its branching properties.

Osteocytes, the most abundant bone cells, have attracted increasing attention of scientists in the recent years. Although their role has been undervalued for a long time, various recent works have evidenced their major role in bone remodeling and repair. As endocrine cells, they could have an impact on many organs¹. For example, osteocytes could be regulators of bone resorption by secreting Receptor activator of NF- κ B ligand (RANKL)² and control bone formation by producing WNT1³. Apart from their function in bone homeostasis, osteocytes may also contribute to fat metabolism by secreting sclerostin, leading to the increase of beige adipogenesis⁴, and influence hematopoiesis by the adjustment of the endosteal microenvironment through the release of soluble factors⁵. After being entrapped in the bone matrix, the mature osteocytes are housed within lacunae and connected to each other by cytoplasmic processes hosted within channels called canaliculi. The porous network hosting the osteocyte system is called the lacuno-canalicular network (LCN). Through the LCN, the osteocytes can transport nutrients, biochemical signals and hormonal stimuli enabling information integration and interaction with other bone cells⁶.

Since the osteocyte system is believed to act as a key regulator of skeletal homeostasis, bone diseases such as osteoporosis, osteoarthritis and osteomalacia were suggested to be associated to disorganized osteocyte networks⁷. Changes of lacunar shapes were observed in osteopenia, osteoporosis and osteoarthritis based on imaging of one sample in human knees⁸. Age related changes have been documented in several studies showing a decrease in the density of lacunae and a loss of dendrites altering the correct communication between osteocytes⁹.

¹Univ Lyon, INSA Lyon, Université Claude Bernard Lyon 1, UJM-Saint Etienne, CNRS UMR 5220, Inserm U1206, CREATIS, 69621, Lyon, France. ²ESRF, the European Synchrotron, 38043, Grenoble, France. *email: francoise.peyrin@creatis.insa-lyon.fr

Nevertheless, the characterization of the LCN remains difficult today due its location embedded within the opaque, mineralized matrix and its complexity. Conventional 2D imaging techniques such as light microscopy^{10,11}, transmission electron microscopy (TEM)¹², scanning electron microscopy (SEM)¹³, and atomic force microscopy (AFM)¹⁴ have been previously used to investigate the LCN. Based on 2D data, lacunae are typically described as flattened ellipsoids with an average area of about 20–70 μm^2 , an average length of about 14–25 μm and an average width of about 5–10 μm ^{15,16}, and the canaliculi are described as channels with an average diameter of about 100–600 nm^{17,18}. However, the 2D measurements present some uncertainty because the slicing direction may bias the results due to missing information about the third dimension.

To overcome this problem, various 3D imaging techniques are explored¹⁹. Confocal laser scanning microscopy (CLSM) has been used to image the LCN by recording a series of 2D optical slices^{20,21}. Recently osteocytes have also been observed with advanced 3D optical techniques such as third harmonic generation imaging²¹, or multiplexed 3D-confocal imaging combining different fluorescent stains²². Serial focused ion beam SEM (serial FIB SEM) is another imaging technique to generate 3D reconstructions of small tissue volumes by collecting a sequence of 2D images while milling the sample layer by layer with a focused ion beam^{23,24}. Besides, it is possible to image the 3D structure of the LCN with Synchrotron Radiation nano-CT (SR nCT) providing an isotropic spatial resolution and a relatively large field of view^{25,26}. The feasibility of ptychographic X-ray CT with synchrotron radiation was also demonstrated²⁷ and recently used to visualize the LCN in rats²⁸. While providing excellent spatial resolution, acquisition time is lengthy and the specimen dimensions have to fit within a reduced field of view.

After imaging, 3D parameters are measured from the images to quantify the LCN. For lacunae, these parameters typically include the lacunar density and porosity, the lacunar volume and surface, the lacunar length, width and depth, the anisotropy and the angle between their long axis and the longitudinal axis of bone^{29–32}. For canaliculi, only few parameters have been described so far. The first parameter of interest is the canalicular porosity volume, which was reported for instance in rodents²³, and more rarely in human³³. The diameter of canaliculi has also been reported from SR nCT images^{33,34}, or ptychographic images²⁸, as well as the number of canaliculi per lacuna^{34,35}. While in the majority of studies the lacunae and canaliculi have been evaluated separately, a recent study used the theory of complex network to assess the LCN in ovine and murine bone³⁶.

Despite the increasing interest in the LCN, data on human bone remains scarce and they are generally limited to a very small number of samples on small fields of view. In addition, the available data come from a large variety of different imaging techniques at different spatial resolutions. Since each imaging modality can generally be used to acquire images at different voxel sizes, the question arises to know which spatial resolution should be used. No study has been dedicated to the effect of spatial resolution on the 3D quantification of the LCN.

In this paper, we explore the possibilities offered by X-ray phase nano-CT associated to automatic image analysis for the 3D quantification of the LCN in human bone samples. The contribution of this work is twofold: we provide new quantitative data on the LCN from 3D images acquired with an isotropic voxel size of 30 nm, and second we study the impact of the spatial resolution on the evaluation of the 3D properties of the LCN. To this aim, we use femoral diaphysis bone samples imaged with 120 nm and 30 nm voxel sizes. We propose a method to quantify and compare the results at the two spatial resolutions. We briefly recall the image analysis techniques used to extract quantitative parameters and present new developments required to handle the volumes at 30 nm. We describe a simple image registration approach to compare the quantitative results between the images at 30 nm and the corresponding registered cropped images at 120 nm. Our results show that the measurements at 120 and 30 nm are strongly correlated in our dataset but that the highest spatial resolution provides more accurate information on the canalicular network and its branching properties.

Methods

Sample description. Bone specimens were harvested from the left femur of seven human cadavers (female, aging 56–95 years old, 75 \pm 15 y.o.). The femurs were provided by the Department of Anatomy, Medical Faculty Rockefeller, University Lyon, France, through the French program on voluntary corpse donation to science. The protocol was approved by the French Ministry of Higher Education and Research (CODECOH “*Conservation d’éléments du corps humain*” number DC-2015–2357). All experiments were carried out in accordance with the approved protocol. The tissue donors or their legal guardians provided informed written consent to give their tissue for investigations, in accord with legal clauses stated in the French Code of Public Health. No additional information regarding donor’s disease or medication history was available following the legal clauses stated in the French Code of Public Health Ethics except for an absence of hepatitis and human immunodeficiency virus. Extracted bones were wrapped in gauze soaked with saline to keep them hydrated, then stored at $-20\text{ }^\circ\text{C}$ until sample preparation. Transverse cross-sections of the femoral diaphysis with a height of 4 mm were first sectioned with a diamond coated blade (Isomet 4000, Buehler, Lyon). The lateral quadrant in each cross section was cut and stored in PBS. Then small samples with a size of $0.4 \times 0.4 \times 4\text{ mm}^3$ were cut using a water-cooled diamond precision saw (Presi Mecatome T210, Struers Diamond Cut-off Wheel EOD15) for nano CT imaging. The samples were then dried with an ascending ethanol solution for 24h, conserved in 70% ethanol and stored at $-4\text{ }^\circ\text{C}$ degrees until synchrotron imaging. We denote the samples by the number #1–7 according to the increasing order of ages.

Synchrotron radiation nano-CT. Imaging was performed using magnified X-ray phase nano-CT at the beamline ID16A of the European Synchrotron Radiation Facility (ESRF) during several sessions of beamtime. This 3D X-ray microscopy technique enables to increase imaging sensitivity thanks to the exploitation of the phase shift of the transmitted wave instead of its attenuation. Image acquisition consisted in repeating four tomographic scans at different focus-to-sample-to-detector distances²⁶. Each bone sample was mounted on a Huber pin and placed on a closed-loop nanopositioning stage inside a vacuum chamber. For each tomographic scan, 2000 angular projections were recorded while rotating the sample over a range of 180° . The energy of the X-ray beam was set either to 17.05 keV or to 33.6 keV with a monochromaticity of 1%. The projections were recorded

on a 2048×2048 lens coupled FreLoN CCD detector. The total acquisition time for one sample scanned at 4 distances was about 4 hours. The 3D images were obtained after processing the recorded projections following two steps: phase retrieval and tomographic reconstruction. Phase retrieval consisted in processing the four projections recorded at the different propagation distances for each rotation angle to obtain a phase map. Following a previous study³⁷, this was performed based on an extended Paganin's algorithm, followed by an iterative optimization. Tomographic reconstruction was then achieved by using the Filtered Back-Projection (FBP) algorithm implemented at the ESRF within the PyHST2 software³⁸. Each bone sample was scanned twice at both 120 nm and 30 nm. The final 3D reconstructed volumes ($2048 \times 2048 \times 2048$ voxels) had a field of view of $61.4 \mu\text{m}$ and $245.8 \mu\text{m}$, respectively at 30 nm and 120 nm. The volumes at 30 nm are denoted by A1–A7, and the site-matched volumes at 120 nm denoted by P1–P7.

Image processing. Image analysis was performed using custom programs. All processing steps were applied to the entire $(2048)^3$ volumes.

Segmentation of the LCN. The segmentation of lacunae and canaliculi was performed sequentially, based on a previously described method that we briefly summarized below³¹.

For the segmentation of lacunae, we first used a median filter to eliminate some speckles, which could be canaliculi or noise, with a physical size smaller than lacunae. Then a hysteresis thresholding method was applied to segment the lacunae from reconstructed volumes and obtain binary images. This method involves two thresholds, a low threshold used to achieve a high-confidence segmentation but with less objects, and a high threshold to refine the results by checking the voxels in the ambiguous region between the two thresholds. Finally, the abnormal structures with huge size corresponding to Haversian canals were filtered out by using connected components analysis.

The automatic segmentation of canaliculi required several steps. We first used a vesselness filter for enhancement of 3D tube-like structures³⁹ to improve the visibility of canaliculi. This method exploits the eigenvalues of the local Hessian matrix at each voxel. The resulting vesselness filter map was then segmented based on maximum entropy thresholding. This binary image was then used as the initialization of a specific region growing method called variational region growing⁴⁰. This method seeks to minimize an energy functional combining gray level information from the original image and shape information from the 3D vesselness filter map to segment canaliculi. This process permits to fill gaps and reconnect some canaliculi. Finally, the smallest connected components were removed to filter out residual noise.

Image registration. To compare the parameters extracted at 30 nm and 120 nm, we registered the corresponding reconstructed images to calculate the parameters on the same volumes of interest (VOIs). Due to our acquisition protocol, we know that the samples did not rotate but were just translated to different positions in the three dimensions, x , y and z . Furthermore, the change in scale is exactly known from the acquisition geometry. Therefore, the registration process is reduced to the estimation of a translation that we addressed by a phase correlation method (PCM), illustrated in Fig. 1.

For a given sample, let us denote $I_1(\mathbf{x})$ and $I_2(\mathbf{x})$ the reconstructed volumes at 120 nm and 30 nm respectively, where $\mathbf{x} = (x, y, z)$ are the 3D coordinates. First, we downsampled the original 2048^3 volume at 30 nm twice in each direction yielding a 512^3 volume with a voxel size of 120 nm, denoted by $I_{2_{DP}}(\mathbf{x})$. Then, this volume was zero-padded to 2048^3 , denoted by $I_{2_{DP}}^*(\mathbf{x})$ and we calculated the phase correlation $p(\mathbf{x})$ between the two volumes as⁴¹:

$$p(\mathbf{x}) = \mathcal{F}^{-1} \left[\frac{\tilde{I}_{2_{DP}}^*(\mathbf{f})\tilde{I}_1(\mathbf{f})}{\left| \tilde{I}_{2_{DP}}^*(\mathbf{f})\tilde{I}_1(\mathbf{f}) \right|} \right] (\mathbf{x}), \quad (1)$$

where $\tilde{I}_1(\mathbf{f})$ is the 3D Fourier transform of $I_1(\mathbf{x})$, $\tilde{I}_{2_{DP}}^*(\mathbf{f})$ the complex conjugate of the Fourier transform of $I_{2_{DP}}(\mathbf{x})$, where $\mathbf{f} = (f_1, f_2, f_3)$ are the spatial frequencies and \mathcal{F}^{-1} the inverse 3D Fourier transform.

The peak intensity of $p(\mathbf{x})$ corresponds to the translation offsets along the three axes (Fig. 1(c)). Using these offsets, we cut a 512^3 volume from the original image $I_1(\mathbf{x})$ at 120 nm. This cropped volume, denoted by $I_{1_{PCM}}(\mathbf{x})$, corresponds to the same region as $I_2(\mathbf{x})$ in the sample and has the same field of view of $61.44 \mu\text{m}$ (Fig. 1(d)).

This process was applied to the seven volumes at the voxel size of 120 nm. The resulting cropped volumes are called here “PCM volumes” and denoted by “P”.

Quantitative analysis. After the segmentation of the LCN, we calculated the same lacunae and canaliculi parameters both for the original volumes at 30 nm and the site-matched volumes at 120 nm.

Quantification of lacunae. We first computed the number of lacunae ($Lc.N$), the total volume of lacunae ($Lc.TV$), the bone volume (BV), the density of lacunae ($Lc.N/BV$) and the lacunar porosity ($Lc.TV/BV$). Then, the segmented image of lacunae was labeled (i.e. assigning one label to each lacuna) and a 3D Voronoi tessellation was performed. This process divides the images into different geometrical patches, where each patch contains only one lacuna⁴². Each patch or Voronoi cell can be interpreted as the local environment of the lacuna. From this information, we measured the average volume of lacuna ($Lc.V$), the average volume of the Voronoi cells ($Cell.V$) and the local lacunar porosity ($Lc.V/Cell.V$).

Moreover, we calculated morphological descriptors of each lacuna by fitting it to an ellipsoid through the second-order moments matrix⁴³. It provided us the length, width and depth of lacuna ($Lc.L_1$, $Lc.L_2$, and $Lc.L_3$), as well as the anisotropy of lacuna described by the ratios between different axes ($Lc.L_1/Lc.L_2$ and $Lc.L_2/Lc.L_3$).

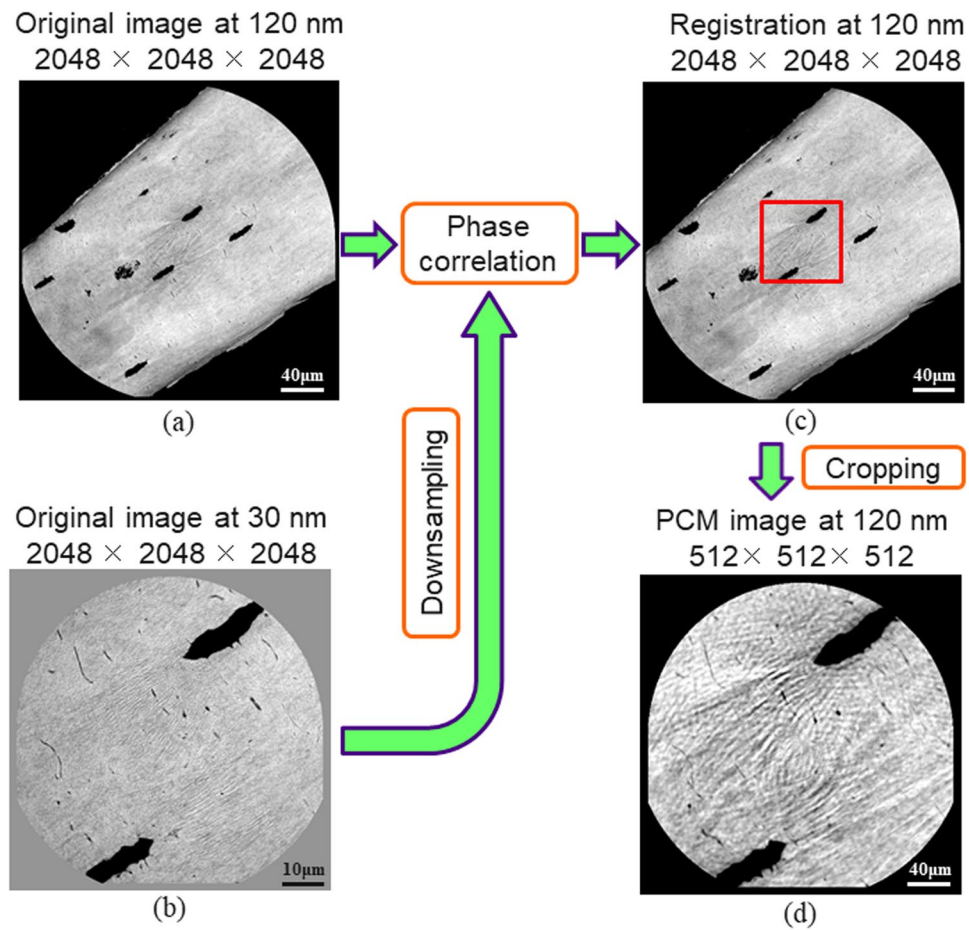


Figure 1. Sketch of the image registration using the phase correlation method. (a) The original image at 120 nm (2048^3 voxels) and (b) the original image at 30 nm (2048^3 voxels) which is first down-sampled (512^3 voxels) are going through phase correlation. (c) The location of the maximum of the result provides the translation between the two images and permits to locate the common area (red square). (d) The 120 nm image is cropped to 512^3 giving the same VOI than the 30 nm.

Besides, we calculated the average surface area of the lacunae ($Lc.S$) and the structure model index of the lacunae ($Lc.SMI$) as described by Ohser⁴⁴.

Quantification of canaliculi. We calculated the total volume of canaliculi ($Ca.TV$), the porosity of canaliculi ($Ca.TV/BV$), the average volume of canaliculi per cell ($Ca.V$), the local porosity of canaliculi measured on the Voronoi cells ($Ca.V/Cell.V$) and the ratio between the average volume of canaliculi and lacunae per cell ($Ca.V/Lc.V$). By adding the lacunae volume, we computed the total volume of the LCN ($LCN.TV$) and the porosity of the LCN ($LCN.TV/BV$) for the evaluation of the whole network. Moreover, to quantify the ramification of canaliculi, we calculated the number of canaliculi per lacuna $Ca.N(r)$ at different distances r from the surface of the lacuna⁴⁵. This calculation was based on the number of holes on the bounding surface. In a previous work of our group⁴⁵, this surface was generated by the numerical dilation of the surface of the segmented lacuna. However, the surface of lacuna at 30 nm contains too many voxels so the 3D dilation becomes very time-consuming. Here, we propose another way to obtain the bounding surface based on the equation of the ellipsoid. An ellipsoid of center $\mathbf{c} = (x_c, y_c, z_c)$ with axis defined by a rotation \mathbf{R} can be expressed by the matrix equation:

$$(\mathbf{x} - \mathbf{c})^T \mathbf{R}^T \mathbf{A} \mathbf{R} (\mathbf{x} - \mathbf{c}) = 1. \quad (2)$$

where $\mathbf{x} = (x, y, z)$ denotes the coordinates of the ellipsoid points and \mathbf{A} is a diagonal matrix coding the length, width and depth of the ellipsoid. Knowing the initial length, width and depth of the ellipsoid, L_1, L_2, L_3 , we can express the isotropic dilation by a factor r of the ellipsoid representing a lacuna, by modifying the matrix \mathbf{A} as:

$$\mathbf{A} = \begin{pmatrix} 1/(L_1/2 + r)^2 & 0 & 0 \\ 0 & 1/(L_2/2 + r)^2 & 0 \\ 0 & 0 & 1/(L_3/2 + r)^2 \end{pmatrix}, \quad (3)$$

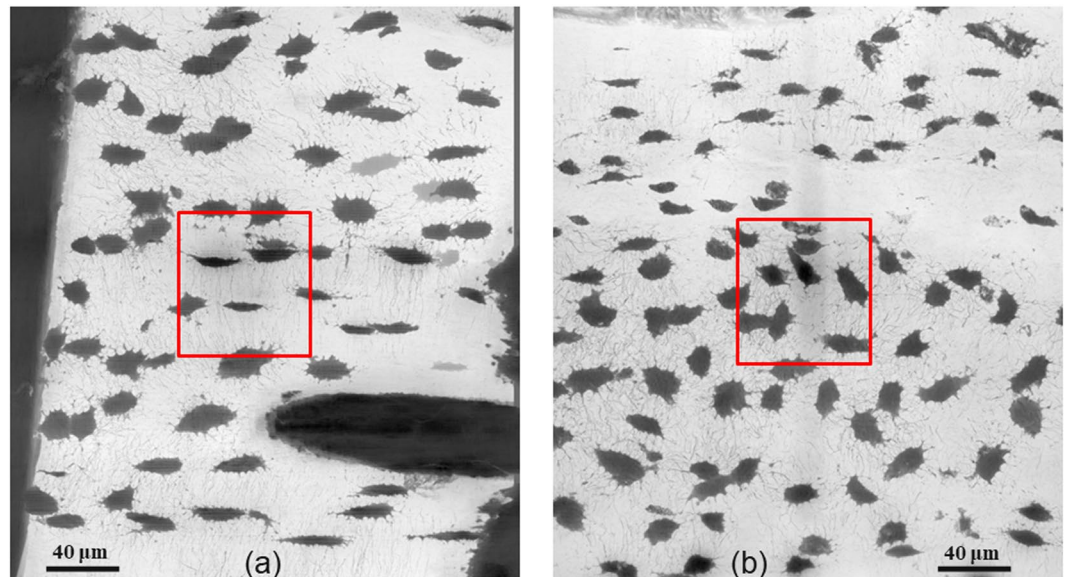


Figure 2. Illustration of the Minimum intensity projections along the Y-axis for samples #1 (left) and #5 (right) at 120 nm showing the full Field of View. The projection depth is 512 voxels i.e. 61.4 μm . The red square illustrates the VOI of the image at 30 nm.

In our case, the length, width and depth of the ellipsoid and the column vectors of the rotation matrix \mathbf{R} were estimated from the eigenvalues and eigenvectors of the second-order moment matrix³¹. Therefore, the dilated lacunae surface can be expressed analytically by Eq. (3) thus reducing computing time. This virtual dilatation was performed for seven increasing values of r from 1.2 μm to 12 μm to obtain the evolution of the number of canaliculi at different distances from the lacunae surface.

In addition, we computed the ratio between the number of canaliculi per lacuna and the surface area of lacuna located in the same cell ($Ca.N/Lc.S$) in order to quantify the density of canaliculi.

Statistical analysis. We used the software Statview[®] (SAS Institute Inc., Cary, NC, USA) for the statistical analysis. We tested if each parameter was different when computed from the 30 nm image or the corresponding PCM one. First the Kolmogorov-Smirnov (K-S) test was used to assess the normality and the F -test to determine the homogeneity of variances. When these conditions were verified, the paired t -test was used to test the difference between the two groups. If the conditions were not verified, the results were statistically tested by the Wilcoxon signed rank test. Besides, we used the Spearman correlation coefficient (R^2) and the p -value by the Fisher's r to z transformation to evaluate correlations between the measured parameters. Results with p -values under 0.05 were considered as significant.

Results

Image Processing. Figure 1 illustrates the results of image registration. Figure 1(a,b) show slices from the original input images ($2048 \times 2048 \times 2048$ voxels) at 120 nm and 30 nm voxel sizes, respectively. Figure 1(b) indicates the position of the cropped region within a slice at 120 nm. Figure 1(d) shows a slice of the cropped volume at 120 nm ($512 \times 512 \times 512$ voxels) restricted to the region of interest. The comparison of Fig. 1(b,d) shows that the phase correlation method finds the accurate position of the VOI in the image at 120 nm, corresponding to that in the image at 30 nm.

Figure 2(a,b) show the Minimum Intensity Projections (MIPs) calculated on 512 slices along the Y-axis for two volumes at 120 nm (samples #1 and #5). The area corresponding to the position of the volume at 30 nm is overlaid in red. Figure 3 displays the MIPs of the registered regions at 120 nm (left) and 30 nm (right) for sample #1 ((a) and (b)) and sample #5 ((c) and (d)). Comparing Fig. 3(a–d), it can be observed that for the same VOI, we obtain a better detection and segmentation of canaliculi at 30 nm voxel size compared with 120 nm. The 3D visualizations of the segmented lacunae and canaliculi rendered by VGStudioMax[®] are displayed in Fig. 4(a) (at 120 nm) and (b), (at 30 nm) respectively. We also provide movies in supplementary materials. Two movies show the 400 middle slices in volume A1 and the corresponding 100 middle slices in volume of P1 sharing the same field of view (see Supplementary Videos S1 and S2). Two other movies present 3D renderings of the entire segmented volumes A1 and P1 (see Supplementary Videos S3 and S4).

Quantitative results at 30 nm. Table 1 reports the average and standard deviation of the morphometric parameters of lacunae calculated the seven samples at 30 nm. The average lacunar porosity was 1.10%. The average volume of each Voronoi cell was $2.6 \times 10^4 \mu\text{m}^3$ and the ratio between the average volume of each lacuna and its enclosing cell was 1.61%. Table 2 shows the parameters measured on canaliculi in each sample ($n = 7$) at 30 nm. We can see that the average canaliculi porosity was 0.35%, and that the total LCN porosity was 1.45%. The average volume of canaliculi per cell is $115.3 \mu\text{m}^3$ with a local canaliculi porosity of 0.48%. The ratio between the

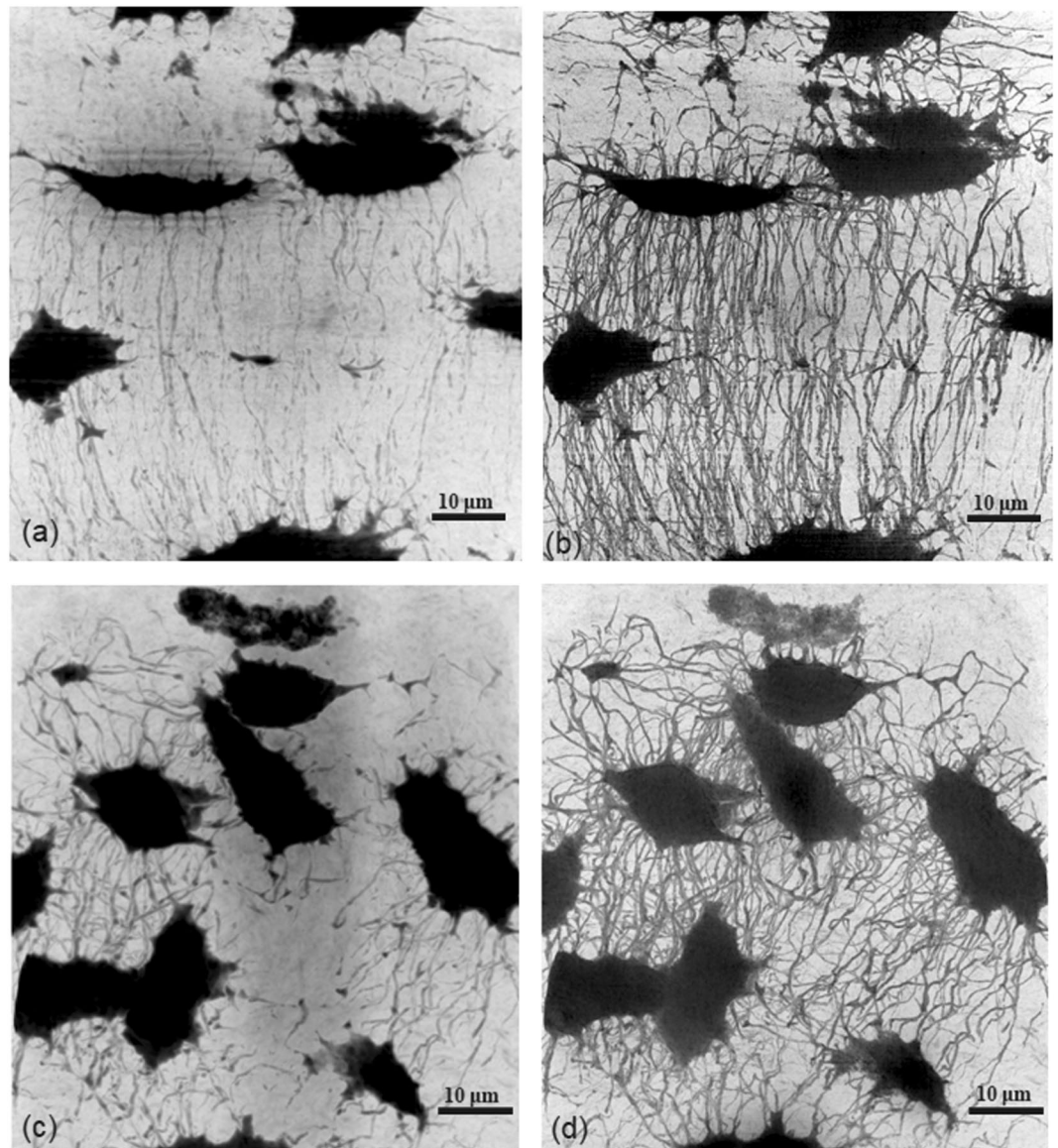


Figure 3. Minimum intensity projections along the Y-axis of the same VOI at 120 nm (left) and 30 nm (right). Top (a,b): sample #1 Bottom (c,d): sample #5.

volume of canaliculi and corresponding lacunae in the same Voronoi cell is 37.7% on average. Table 3 displays the quantitative results of the ramification of canaliculi. These parameters permit to assess the number of canaliculi issued from each lacuna and follow its evolution at different distances from the lacunar surface. The results show that average number of canaliculi per lacuna increases from 79.7 to 114.5. The corresponding density of canaliculi in the same cell also increases from $0.21 \mu\text{m}^{-2}$ to $0.32 \mu\text{m}^{-2}$.

Quantification of cropped volumes at 120 nm. The same analysis was performed on the seven registered and cropped volumes at 120 nm voxel size. Table 1 also presents the lacunae parameters calculated from the cropped volumes. The average number of lacunae and density of lacunae are unchanged compared to 30 nm. The average lacunar porosity was 1.01%. Table 2 also shows the morphometric canaliculi parameters for the cropped volumes at 120 nm. The canaliculi porosity was 0.30% on average and the total LCN porosity was 1.31%. The average volume of canaliculi per Voronoi cell was $97.2 \mu\text{m}^3$ with a local canaliculi porosity of 0.41%. In addition, the average ratio between the canaliculi and lacuna volume within the same Voronoi cell was 34.5%. Table 3 displays the quantitative results of the ramification of canaliculi at the same seven distances from the lacuna surface as at 30 nm.

Comparison of parameters on matched VOIs at 30 nm and 120 nm. The average relative difference between parameters measured at 30 nm and 120 nm are reported in Tables 1–3.

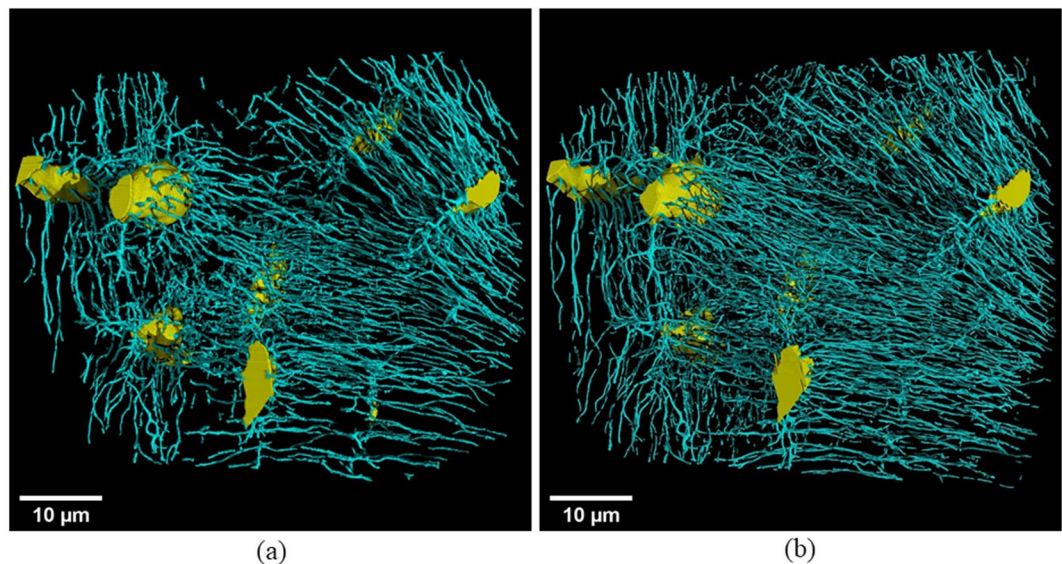


Figure 4. 3D renderings of the segmented lacunae and canaliculi corresponding to sample #1 at 120 nm (left) and 30 nm (right).

	Lc.N	Lc.TV* (10^{-5} mm^3)	BV (10^{-3} mm^3)	Lc.TV/BV* (%)	Lc.N/BV (10^4 mm^{-3})	Lc.V* (μm^3)	Cell.V ($10^4 \mu\text{m}^3$)	Lc.V/Cell.V* (%)
30 nm	5.3 ± 2.1	0.18 ± 0.08	0.17 ± 0.02	1.10 ± 0.48	3.2 ± 1.2	347.8 ± 61.4	2.62 ± 0.65	1.61 ± 0.54
120 nm (pcm)	5.3 ± 2.1	0.17 ± 0.07	0.17 ± 0.02	1.01 ± 0.44	3.2 ± 1.2	315.6 ± 51.7	2.6 ± 0.6	1.47 ± 0.51
Diff	—	8.9%	—	8.9%	—	8.9%	0.9%	9.0%
	Lc.S* (μm^2)	Lc.L1* (μm)	Lc.L2* (μm)	Lc.L3* (μm)	Lc.L1/Lc.L2	Lc.L2/Lc.L3	Lc.SMI	
30 nm	369.7 ± 57.3	17.2 ± 1.8	9.4 ± 1.1	4.8 ± 0.7	1.9 ± 0.3	2.1 ± 0.5	3.1 ± 0.3	
120 nm (pcm)	326.0 ± 50.0	16.7 ± 1.7	9.0 ± 1.0	4.6 ± 0.7	2.0 ± 0.3	2.1 ± 0.5	3.1 ± 0.3	
Diff	11.7%	3.2%	3.7%	3.6%	0.9%	2.5%	1.9%	

Table 1. Morphometric parameters of lacunae at different voxel sizes. Lc.N – number of lacunae Lc.TV – total volume of lacunae (mm^3). BV – bone volume (mm^3) Lc.TV/BV – lacunar porosity (%). Lc.N/BV – density of lacunae (mm^{-3}) Lc.V – average volume of lacuna (μm^3). Cell.V – average volume of each Voronoi cell (μm^3) Lc.S – average surface area of lacuna (μm^2). Lc.V/Cell.V – local lacunar porosity (%) Lc.SMI – average structural model index of lacuna. Lc.L1, Lc.L2 and Lc.L3 – average length, width and depth of lacuna (μm). Lc.L1/Lc.L2 and Lc.L2/Lc.L3 – average anisotropy of lacuna. * p -value < 0.05.

	Ca.TV* (10^{-5} mm^3)	LCN.TV* (10^{-5} mm^3)	Ca.TV/BV* (%)	LCN.TV/BV (%)	Ca.V* (μm^3)	Ca.V/Cell.V* (%)	Ca.V/Lc.V (%)
30 nm	0.06 ± 0.03	0.24 ± 0.10	0.35 ± 0.16	1.45 ± 0.57	115.3 ± 45.8	0.48 ± 0.20	37.7 ± 16.3
120 nm (pcm)	0.05 ± 0.03	0.22 ± 0.09	0.30 ± 0.16	1.31 ± 0.55	97.2 ± 48.3	0.41 ± 0.19	34.5 ± 16.1
Diff	17.6%	10.9%	17.6%	10.9%	17.6%	15.0%	10.7%

Table 2. Morphometric parameters of canaliculi at different voxel sizes. Ca.TV – total volume of canaliculi (mm^3) LCN.TV – total volume of the LCN (mm^3). Ca.TV/BV – porosity of canaliculi (%) LCN.TV/BV – porosity of the LCN (%). Ca.V – average volume of canaliculi per cell (μm^3) Ca.V/Cell.V – local porosity of canaliculi. Ca.V/Lc.V – ratio between the average volume of canaliculi and lacuna per cell (%). * p -value < 0.05.

Figure 5 illustrates the values of lacunae sizes, $Lc.L_1$, $Lc.L_2$, $Lc.L_3$ imaged at 30 nm and 120 nm, showing a slight increase of parameter values at 30 nm compared to 120 nm. Figure 6 shows the average number of canaliculi per lacuna and the average density of canaliculi as a function of the distance to the surface of lacunae.

Table 4 shows the Spearman correlation coefficients and the corresponding p -values between the parameters from the same VOIs at 30 nm and 120 nm. We wanted to check whether there are good correlations ($R^2 > 0.5$ and $p < 0.05$) between these parameters quantified at different voxel sizes. For the parameters quantified from the volumes at 30 nm and the PCM ones, all the parameters passed the test of the homogeneity of variances. Therefore, we used the paired t -test for the evaluation of parameters. Between the two groups, there were no significant differences for the $Lc.N/BV$, $Cell.V$, $Lc.L_1/Lc.L_2$, $Lc.L_2/Lc.L_3$, $Lc.SMI$, $Ca.V/Lc.V$. However, the results of $Lc.TV/BV$,

	Ca.N* (r = 1.2 μm)	Ca.N* (r = 3.0 μm)	Ca.N* (r = 4.8 μm)	Ca.N* (r = 6.6 μm)	Ca.N* (r = 8.4 μm)	Ca.N* (r = 10.2 μm)	Ca.N* (r = 12.0 μm)
30 nm	79.7 ± 19.2	82.7 ± 25.6	86.2 ± 29.8	85.9 ± 37.8	90.2 ± 42.6	100.0 ± 47.1	114.2 ± 57.3
120 nm (pcm)	49.7 ± 15.1	47.9 ± 19.9	49.8 ± 24.5	48.7 ± 25.6	47.2 ± 26.5	47.7 ± 27.9	49.1 ± 34.1
Diff	38.8%	44.4%	46.9%	48.8%	52.2%	56.5%	60.9%
	Ca.N/Lc.S* (μm ⁻² , r = 1.2 μm)	Ca.N/Lc.S* (μm ⁻² , r = 3.0 μm)	Ca.N/Lc.S* (μm ⁻² , r = 4.8 μm)	Ca.N/Lc.S* (μm ⁻² , r = 6.6 μm)	Ca.N/Lc.S* (μm ⁻² , r = 8.4 μm)	Ca.N/Lc.S* (μm ⁻² , r = 10.2 μm)	Ca.N/Lc.S* (μm ⁻² , r = 12.0 μm)
30 nm	0.21 ± 0.05	0.22 ± 0.07	0.23 ± 0.08	0.23 ± 0.10	0.24 ± 0.11	0.27 ± 0.12	0.32 ± 0.14
120 nm (pcm)	0.16 ± 0.05	0.15 ± 0.07	0.16 ± 0.08	0.16 ± 0.08	0.15 ± 0.08	0.15 ± 0.08	0.16 ± 0.10
Diff	27.9%	34.7%	38.2%	39.4%	43.2%	49.4%	53.8%

Table 3. Number of canaliculi per lacuna at 7 different distances from the surface of the lacuna and density of canaliculi at different voxel sizes. Ca.N – number of canaliculi per lacuna Ca.N/Lc.S – density of canaliculi. **p*-value < 0.05.

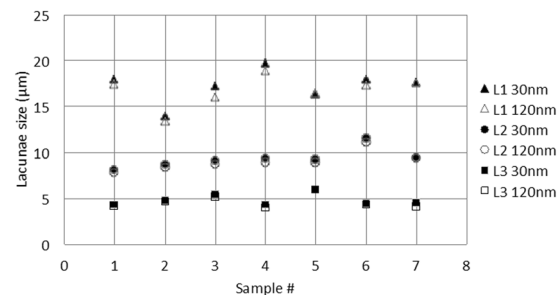


Figure 5. Plot of lacunae sizes Lc.L₁, Lc.L₂, Lc.L₃ measured at 30 nm (black) and 120 nm (white) for the different samples.

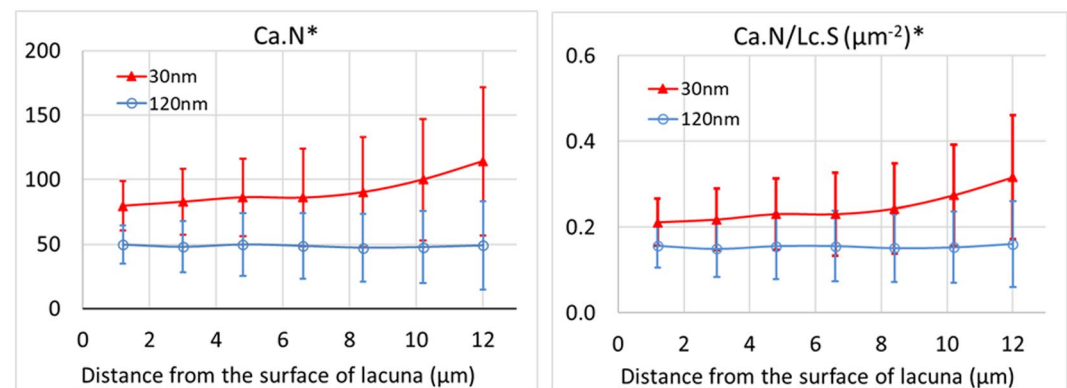


Figure 6. Plot of the evolution at different distances of the number of canaliculi *Ca.N* (left) and the density of canaliculi per lacunae surface *Ca.N/Lc.S* (right) at 30 nm (triangle) and 120 nm (circle) (**p*-value < 0.05).

Lc.V, *Lc.V/Cell.V*, *Lc.S*, *Lc.L₁*, *Lc.L₂*, *Lc.L₃*, *LCN.TV/BV*, *Ca.TV/BV*, *Ca.V*, *Ca.V/Cell.V*, *Ca.N* and *Ca.N/Lc.S* at 30 nm were significantly different from those of the PCM volumes (*p*-value < 0.05).

Besides, we give the quantitative results for all the reconstructed volumes at 30 nm and the cropped volumes at 120 nm in Supplementary Tables S1 and S2, respectively. To check the ramification of canaliculi, we also show the plots of *Ca.N* and *Ca.N/Lc.S* for all the volumes at different voxel sizes in Supplementary Figs. S1 and S2.

Discussion

This work reports quantitative parameters of the LCN from X-ray phase nano-CT images at two voxel sizes and assesses the effect of the spatial resolution by comparing results obtained from registered images. A voxel size of 30 nm is the highest spatial resolution that has ever been reported for the analysis of human bone samples by using this technique, even if similar spatial resolution can be reached for instance from ptychography²⁸ or FIB/SEM techniques²³. Nevertheless, the effect of the improved spatial resolution in terms of the quantitative assessment of the LCN needed to be clarified. Our data at two spatial resolutions permitted to address this question by comparing results on site-matched volumes of the same samples. Due to the acquisition protocol ensuring a scaled, rigid transformation without rotation between the two images, the phase correlation method was found suitable to register corresponding 3D images.

Parameter	Slope	R ²	p-value
Lc.TV/BV	0.9198	0.9951	<0.0001
Lc.V	0.8300	0.9710	<0.0001
Lc.S	0.8207	0.8849	0.0016
Lc.V/Cell.V	0.9313	0.9755	<0.0001
Lc.L1	0.9483	0.9470	0.0002
Lc.L2	0.9249	0.9885	<0.0001
Lc.L3	1.0384	0.9713	<0.0001
Ca.TV/BV	0.9459	0.9594	0.0001
LCN.TV/BV	0.9476	0.9964	<0.0001
Ca.V	0.9979	0.8955	0.0012
Ca.V/Cell.V	0.9514	0.9542	0.0002
Ca.V/Lc.V	0.9398	0.9038	0.0010

Table 4. Spearman correlation detection between parameters from the volumes at the voxel size of 30 nm and the cropped ones at 120 nm.

In total, 7 human femoral diaphysis samples were analyzed with an average of 5.3 lacunae per sample. This analysis was performed using a custom-made automatic digital image analysis program enabling to binarize the LCN and extract a number of 3D parameters. Most of the previous findings on the LCN were based on image analysis tools requiring human interaction. While this can be performed easily on few 2D images with small fields of view, scaling up to 3D images of $2048 \times 2048 \times 2048$ voxels as in our study becomes incompatible with manual segmentation and quantification. It would require lengthy and tedious human work to delineate lacunae and canaliculi, likely with limited accuracy, and the extraction of 3D measurements from a stack of slices is not straightforward. All our parameters were measured directly in 3D space and we proposed new parameters such as those characterizing the local porosity around each lacuna using Voronoi tessellation.

The density of lacunae was found to be $32\,000\text{ mm}^{-3}$ and was not affected by the voxel size. The results are in the range of previous studies for the density ($10,000\text{--}35,000\text{ mm}^{-3}$)^{30,31,46–48}. Concerning the morphological properties of lacunae, the average volume (*Lc.V*) and surface area (*Lc.S*) of lacuna at 30 nm were respectively $347.8\ \mu\text{m}^3$ and $369.7\ \mu\text{m}^2$. The average length, width and depth of lacuna (*Lc.L1*, *Lc.L2* and *Lc.L3*) at 30 nm were $17.2\ \mu\text{m}$, $9.4\ \mu\text{m}$, $4.8\ \mu\text{m}$. All parameters are consistent with previous works^{8,31,47,49}. For instance the lacunar volumes *Lc.V* are found in a range varying from 50 to $730\ \mu\text{m}^3$ ^{15,30}. The lacunar surface was previously reported to be $336.2 \pm 94.5\ \mu\text{m}^2$ in the work of Dong³¹ and $430.4 \pm 68.5\ \mu\text{m}^2$ in that of Varga³⁴. There are however fluctuations that can be attributed to species or site location.

The present work provides data on the micro porosity related to the LCN in human bone including both the lacunae and the canaliculi network imaged at a very high spatial resolution. The lacunar porosity (*Lc.TV/BV*) was found to be 1.10% and the canalicular porosity (*Ca.TV/BV*) was 0.35%, providing an average LCN porosity of 1.45%. The LCN porosity was underestimated in average by 11% at 120 nm mainly due to the loss of the thinnest canaliculi (see Fig. 4(a,b)). The lacunar porosity has been assessed in human cortical bone in previous works providing a similar range in human tissue^{30,31}. There are only few reports on the canalicular porosity, especially measured in 3D in human bones. For instance, Ashique¹⁶ reported a canalicular area percentage between 7.9% and 14.3% in human femora but the use of confocal microscopy is likely to overestimate the values. Our values of *Ca.TV/BV* are comparable to those measured from SR imaging reported in previous works 0.57%³⁴, 2%³³. However, Varga³⁴ calculated the porosity of canaliculi around specific lacunae instead of covering the whole volume; Hesse³³ measured porosity in human jaw bone under different health conditions. We also measured the relative ratio of canalicular to lacunar volume, which was found to be 37.7% in average.

We also introduced new parameters to quantify the local porosity of the lacunae and canaliculi within their corresponding Voronoi cells. The average volume of each Voronoi cell (*Cell.V*) was found to be $26000\ \mu\text{m}^3$. The average volume of canaliculi per cell (*Ca.V*) at 30 nm voxel size was $115.3\ \mu\text{m}^3$. The local porosity of the lacunae and canaliculi (*Lc.V/Cell.V* and *Ca.V/Cell.V*) at 30 nm were 1.61% and 0.48%, respectively. These parameters provide data about the density of canaliculi in the neighborhood of each lacuna, giving information about fluid exchanges in this neighborhood.

Another new information from this work is the evaluation of the number of canaliculi per lacuna which was computed at seven distances from the surface of lacuna ranging from $1.2\ \mu\text{m}$ to $12.0\ \mu\text{m}$. The results show that the average number of canaliculi per lacuna (*Ca.N*) measured at 30 nm increases progressively from 79.7 to 114.2 as shown in Fig. 6(a). This increase is less apparent at 120 nm since the narrowest canaliculi may not be resolved. Varga *et al.* has reported a number of canaliculi per lacuna in the range 53–126, but using only a fixed distance³⁴. Dong *et al.* has also found an increase of the average number of canaliculi per lacuna from 41.5 to 139.1 in the same range of distances⁴⁵. Our results are consistent with this study but our growth rate of *Ca.N* seems to be lower. However, in this previous work, the analysis was performed on a single sample imaged at 300 nm while our study includes 7 samples imaged at 30 nm. The first report of the number of primary canaliculi was an estimation derived from a model and using values of the literature⁵⁰, thus not from direct observations. More recently measurements were reported in rats using confocal microscopy⁵¹ and ptychography²⁸. The ratio between the number of canaliculi per lacuna and the surface area of lacuna (*Ca.N/Lc.S*) describing a local density of canaliculi increases progressively from $0.21\ \mu\text{m}^{-2}$ at $1.2\ \mu\text{m}$ to $0.32\ \mu\text{m}^{-2}$ at $12.0\ \mu\text{m}$ (30 nm voxel size), while on the PCM volumes it fluctuates around $0.16\ \mu\text{m}^{-2}$ (see Fig. 6(b)). These results are consistent with previous reports of the

density of canaliculi $0.18 \pm 0.03 \mu\text{m}^{-2}$ or $0.21 \pm 0.05 \mu\text{m}^{-2}$ for mice samples^{35,52}. The estimation of the number of canaliculi is an important parameter for the modeling of fluid flow transport and permeability measurements^{49,50}.

The measurements at 30 nm were compared to those made on site-matched registered volumes acquired at 120 nm. Concerning the morphological properties of lacunae, the average volume ($Lc.V$) and surface ($Lc.S$) of lacunae at 30 nm, of respectively $347.8 \mu\text{m}^3$ and $369.7 \mu\text{m}^2$, were bigger than those measured at 120 nm ($315.6 \mu\text{m}^3$ and $326.0 \mu\text{m}^2$). The average length, width and depth of lacunae ($Lc.L1$, $Lc.L2$, and $Lc.L3$) at 30 nm were slightly larger with differences smaller than $0.5 \mu\text{m}$ than those evaluated at 120 nm. Nevertheless, we found very high Spearman correlation coefficients ($R^2 > 0.9$) for all lacunae parameters. Compared to the average size of lacunae, a voxel size of 120 nm is sufficient to measure lacunae properties. The significant differences found on the lacunae volume, surface and sizes are likely to be related to the inclusion of canaliculi junctions in the segmented lacunae at 30 nm. This introduces small protuberances on the lacunae surface, which slightly modifies the measurements and could be avoided by smoothing the lacunae surface. Besides, the selected thresholds had impact on the segmented results although we have used hysteresis thresholding to refine the segmentation. The shape and anisotropy of lacunae were the same at 30 nm and 120 nm. The values of $Lc.SMI$, quantifying the global shape of the sample did not change with the resolution and are consistent with previous reports: 3.1³¹. The average ratios between the length, the width and the depth are both close to 4:2:1 for the two resolutions.

The visual observation of the LCN as illustrated on the 3D rendering of Fig. 4 does not permit to appreciate clearly the differences in the network. However, most canaliculi parameters were affected by the decrease of spatial resolution. The quantitative analysis of canaliculi demonstrates clearly that there is a loss in the canaliculi volume and numbers of canaliculi. The ratio $Ca.V/Lc.V$ at 30 nm was also higher (37.7%) than the one quantified at 120 nm (34.5%). At all the seven distances, the average number and density of canaliculi ($Ca.N$ and $Ca.N/Lc.S$) were significantly different at 30 and 120 nm. This shows that we achieved more accurate segmentation and quantification of canaliculi using the volumes at 30 nm. Thus, the high spatial resolution images yield more accurate investigation results of canaliculi thanks to better resolving power matching their tiny physical diameter ($\sim 200\text{--}500 \text{ nm}$)^{34,49}.

Although we can better observe and quantify canaliculi at 30 nm, the measurements are limited to a small region of interest (currently $61.4 \mu\text{m}$ in the three directions). The complementary observation of the LCN in the 120 nm images offering a larger field of view with a volume 64 times larger permits to have more insight on the localization of the VOI analyzed at 30 nm. Most VOIs were located in osteonal tissue but one sample was at the frontier with interstitial tissue, clearly showing a different organization with an obvious decrease of lacunae and canaliculi. Thus, although the images at 120 nm definitely miss canaliculi, they provide a more global observation of the sample. This scale can thus be particularly interesting to analyze organized versus disorganized LCN in human disease or animal models. In perspective, the implementation of techniques such as correlative microscopy could help with the selection of the zoom-in VOI at 30 nm within the larger field of view, and the increase of the detector size could permit to increase the field of view at 30 nm.

This study has some limitations. First, the quantitative results on the LCN were obtained from seven samples, which remains a limited number. Nevertheless, we could observe a large variability in the LCN within this population and there are few comparable data on human tissue in the literature. In perspective, we expect to quantify a larger number of samples from normal and diseased specimens. Second, one limitation related to the imaging technique is that it does not allow seeing the actual cells but only the porous network embedding the cells²². However, our images have an isotropic voxel size, which prevents some bias in measurements like it is recognized to happen in confocal microscopy⁵¹ and the depth of the FOV is not limited by light penetration. Third, although a complete image processing workflow has been used, more research could allow improving the segmentation accuracy of canaliculi, which remains challenging. Therefore, a perspective could be to develop further segmentation methods dedicated to canaliculi by trying to preserve the connectivity of canaliculi without introducing false detections. Finally, one should design additional descriptors to evaluate the properties of the whole network instead of lacunae and canaliculi separately, to better understand the spatial distribution and the topological structure of the LCN.

In conclusion, this work presents an assessment of the lacuno-canalicular in human bone with unprecedented 3D isotropic spatial resolution. The obtained images at 30 nm voxel size provide the most precise measurements to assess the LCN network and the morphology of canaliculi. While the canaliculi parameters are more accurate at 30 nm, a voxel size of 120 nm permits to investigate the 3D properties of the whole network on a larger field of view and may give us apparent parameters that could be meaningful when comparing different populations of samples. Thus, the choice of the 30 nm versus 120 nm voxel size depends on the aim of the study. Overall the technique employed here providing an isotropic spatial resolution may compare favorably to techniques based on visible light imaging. Our results on lacunae are consistent with previous studies and bring direct measurements of canaliculi volume, porosity and count of canaliculi stemming from each lacuna, which have not been previously reported, especially on human bone. It is expected that these quantitative parameters will constitute reference values in the field and will contribute to enhance our knowledge on the bone cell network. The presented methodology also opens new perspectives to assess the LCN in bone disease.

Data availability

The datasets that support the plots within this paper and other findings of this study are available from the corresponding author upon reasonable request.

Received: 5 July 2019; Accepted: 17 February 2020;

Published online: 12 March 2020

References

- Dallas, S. L., Pridaux, M. & Bonewald, L. F. The Osteocyte: An Endocrine Cell ... and More. *Endocr. Rev.* **34**, 658–690 (2013).
- Nakashima, T. *et al.* Evidence for osteocyte regulation of bone homeostasis through RANKL expression. *Nat. Med.* **17**, 1231 (2011).
- Rauch, F. The brains of the bones: how osteocytes use WNT1 to control bone formation. *J. Clin. Invest.* **127**, 2539–2540 (2017).
- Fulzele, K. *et al.* Osteocyte-secreted Wnt signaling inhibitor sclerostin contributes to beige adipogenesis in peripheral fat depots. *J. Bone Miner. Res.* **32**, 373–384 (2017).
- Asada, N., Sato, M. & Katayama, Y. Communication of bone cells with hematopoiesis, immunity and energy metabolism. *BoneKEY Rep.* **4** (2015).
- Bonewald, L. F. The amazing osteocyte. *J. Bone Miner. Res.* **26**, 229–238 (2011).
- Knothe Tate, M. L., Adamson, J. R., Tami, A. E. & Bauer, T. W. The osteocyte. *Int. J. Biochem. Cell Biol.* **36**, 1–8 (2004).
- van Hove, R. P. *et al.* Osteocyte morphology in human tibiae of different bone pathologies with different bone mineral density — Is there a role for mechanosensing? *Bone* **45**, 321–329 (2009).
- Tiede-Lewis, L. M. & Dallas, S. L. Changes in the osteocyte lacunocanalicular network with aging. *Bone* **122**, 101–113 (2019).
- Marotti, G., Ferretti, M., Remaggi, F. & Palumbo, C. Quantitative evaluation on osteocyte canalicular density in human secondary osteons. *Bone* **16**, 125–128 (1995).
- Qiu, S., Rao, D. S., Palnitkar, S. & Parfitt, A. M. Differences in osteocyte and lacunar density between Black and White American women. *Bone* **38**, 130–135 (2006).
- Rubin, M. A. & Jasiuk, I. The TEM characterization of the lamellar structure of osteoporotic human trabecular bone. *Micron* **36**, 653–664 (2005).
- Sasaki, M., Kuroshima, S., Aoki, Y., Inaba, N. & Sawase, T. Ultrastructural alterations of osteocyte morphology via loaded implants in rabbit tibiae. *J. Biomech.* **48**, 4130–4141 (2015).
- Katsamenis, O. L., Chong, H. M. H., Andriotis, O. G. & Turner, P. J. Load-bearing in cortical bone microstructure: Selective stiffening and heterogeneous strain distribution at the lamellar level. *J. Mech. Behav. Biomed. Mater.* **17**, 152–165 (2013).
- Remaggi, F., Canè, V., Palumbo, C. & Ferretti, M. Histomorphometric study on the osteocyte lacuno-canalicular network in animals of different species. I. Woven-fibered and parallel-fibered bones. *Ital. J. Anat. Embryol. Arch. Ital. Anat. Ed Embriologia* **103**, 145–155 (1998).
- Ashique, A. M. *et al.* Lacunar-canalicular network in femoral cortical bone is reduced in aged women and is predominantly due to a loss of canalicular porosity. *Bone Rep.* **7**, 9–16 (2017).
- You, L.-D., Weinbaum, S., Cowin, S. C. & Schaffler, M. B. Ultrastructure of the osteocyte process and its pericellular matrix. *Anat. Rec.* **278A**, 505–513 (2004).
- Lin, Y. & Xu, S. AFM analysis of the lacunar-canalicular network in demineralized compact bone: Afn For 3D Tissue Nanostructure. *J. Microsc.* **241**, 291–302 (2011).
- Schneider, P., Meier, M., Wepf, R. & Müller, R. Towards quantitative 3D imaging of the osteocyte lacuno-canalicular network. *Bone* **47**, 848–858 (2010).
- Kamioka, H., Honjo, T. & Takano-Yamamoto, T. A three-dimensional distribution of osteocyte processes revealed by the combination of confocal laser scanning microscopy and differential interference contrast microscopy. *Bone* **28**, 145–149 (2001).
- Genthial, R. *et al.* Label-free imaging of bone multiscale porosity and interfaces using third-harmonic generation microscopy. *Sci. Rep.* **7** (2017).
- Kamel-ElSayed, S. A., Tiede-Lewis, L. M., Lu, Y., Veno, P. A. & Dallas, S. L. Novel approaches for two and three dimensional multiplexed imaging of osteocytes. *Bone* **76**, 129–140 (2015).
- Schneider, P., Meier, M., Wepf, R. & Müller, R. Serial FIB/SEM imaging for quantitative 3D assessment of the osteocyte lacuno-canalicular network. *Bone* **49**, 304–311 (2011).
- Hasegawa, T. *et al.* Three-dimensional ultrastructure of osteocytes assessed by focused ion beam-scanning electron microscopy (FIB-SEM). *Histochem. Cell Biol.* <https://doi.org/10.1007/s00418-018-1645-1> (2018).
- Pacureanu, A., Langer, M., Boller, E., Tafforeau, P. & Peyrin, F. Nanoscale imaging of the bone cell network with synchrotron X-ray tomography: optimization of acquisition setup: Synchrotron x-ray tomography reveals the bone cell network. *Med. Phys.* **39**, 2229–2238 (2012).
- Langer, M. *et al.* X-Ray Phase Nanotomography Resolves the 3D Human Bone Ultrastructure. *PLoS One* **7**, e35691 (2012).
- Dierolf, M. *et al.* Ptychographic X-ray computed tomography at the nanoscale. *Nature* **467**, 436–439 (2010).
- Ciani, A. *et al.* Ptychographic X-ray CT characterization of the osteocyte lacuno-canalicular network in a male rat's glucocorticoid induced osteoporosis model. *Bone Rep.* **9**, 122–131 (2018).
- Mader, K. S., Schneider, P., Müller, R. & Stapanoni, M. A quantitative framework for the 3D characterization of the osteocyte lacunar system. *Bone* **57**, 142–154 (2013).
- Carter, Y., Thomas, C. D. L., Clement, J. G. & Cooper, D. M. L. Femoral osteocyte lacunar density, volume and morphology in women across the lifespan. *J. Struct. Biol.* **183**, 519–526 (2013).
- Dong, P. *et al.* 3D osteocyte lacunar morphometric properties and distributions in human femoral cortical bone using synchrotron radiation micro-CT images. *Bone* **60**, 172–185 (2014).
- Bach-Gansmo, F. L. *et al.* Osteocyte lacunar properties in rat cortical bone: Differences between lamellar and central bone. *J. Struct. Biol.* **191**, 59–67 (2015).
- Hesse, B. *et al.* Canalicular Network Morphology Is the Major Determinant of the Spatial Distribution of Mass Density in Human Bone Tissue: Evidence by Means of Synchrotron Radiation Phase-Contrast nano-CT. *J. Bone Miner. Res.* **30**, 346–356 (2015).
- Varga, P. *et al.* Synchrotron X-ray phase nano-tomography-based analysis of the lacunar-canalicular network morphology and its relation to the strains experienced by osteocytes *in situ* as predicted by case-specific finite element analysis. *Biomech. Model. Mechanobiol.* **14**, 267–282 (2015).
- Lai, X. *et al.* The dependences of osteocyte network on bone compartment, age, and disease. *Bone Res.* **3** (2015).
- Kollmannsberger, P. *et al.* The small world of osteocytes: connectomics of the lacuno-canalicular network in bone. *New J. Phys.* **19**, 073019 (2017).
- Yu, B. *et al.* Evaluation of phase retrieval approaches in magnified X-ray phase nano computerized tomography applied to bone tissue. *Opt. Express* **26**, 11110 (2018).
- Mirone, A., Brun, E., Gouillart, E., Tafforeau, P. & Kieffer, J. The PyHST2 hybrid distributed code for high speed tomographic reconstruction with iterative reconstruction and a priori knowledge capabilities. *Nucl. Instrum. Methods Phys. Res. Sect. B Beam Interact. Mater. At.* **324**, 41–48 (2014).
- Sato, Y. *et al.* Three-dimensional multi-scale line filter for segmentation and visualization of curvilinear structures in medical images. *Med. Image Anal.* **2**, 143–168 (1998).
- Pacureanu, A., Revol-Muller, C., Rose, J.-L., Ruiz, M. S. & Peyrin, F. Vesselness-guided variational segmentation of cellular networks from 3D micro-CT. In *2010 IEEE International Symposium on Biomedical Imaging: From Nano to Macro* 912–915 (IEEE, 2010).
- Foroosh, H., Zerubia, J. B. & Berthod, M. Extension of phase correlation to subpixel registration. *IEEE Trans. Image Process.* **11**, 188–200 (2002).
- Zuluaga, M. A. *et al.* Bone canalicular network segmentation in 3D nano-CT images through geodesic voting and image tessellation. *Phys. Med. Biol.* **59**, 2155–2171 (2014).
- Flusser, J., Suk, T. & Zitov, B. *Moments and moment invariants in pattern recognition.* (J. Wiley, 2009).

44. Ohser, J. & Schloditz, K. *3D images of materials structures: processing and analysis*. (Wiley-VCH, 2009).
45. Dong, P. *et al.* Quantification of the 3D morphology of the bone cell network from synchrotron micro-CT images. *Image Anal. Stereol.* **33**, 157 (2014).
46. Bach-Gansmo, F. L. *et al.* Osteocyte lacunar properties and cortical microstructure in human iliac crest as a function of age and sex. *Bone* **91**, 11–19 (2016).
47. Andronowski, J. M., Mundorff, A. Z., Pratt, I. V., Davoren, J. M. & Cooper, D. M. L. Evaluating differential nuclear DNA yield rates and osteocyte numbers among human bone tissue types: A synchrotron radiation micro-CT approach. *Forensic Sci. Int. Genet.* **28**, 211–218 (2017).
48. Gauthier, R. *et al.* 3D micro structural analysis of human cortical bone in paired femoral diaphysis, femoral neck and radial diaphysis. *J. Struct. Biol.* **204**, 182–190 (2018).
49. Gatti, V., Azoulay, E. M. & Fritton, S. P. Microstructural changes associated with osteoporosis negatively affect loading-induced fluid flow around osteocytes in cortical bone. *J. Biomech.* **66**, 127–136 (2018).
50. Beno, T., Yoon, Y.-J., Cowin, S. C. & Fritton, S. P. Estimation of bone permeability using accurate microstructural measurements. *J. Biomech.* **39**, 2378–2387 (2006).
51. Sharma, D. *et al.* Alterations in the osteocyte lacunar-canalicular microenvironment due to estrogen deficiency. *Bone* **51**, 488–497 (2012).
52. Wang, L. *et al.* *In situ* measurement of solute transport in the bone lacunar-canalicular system. *Proc. Natl. Acad. Sci.* **102**, 11911–11916 (2005).

Acknowledgements

This work was done in the framework of LabEx PRIMES ANR-11-LABX-006 of Université de Lyon and in the context of the ANR MULTIPS project (ANR-13-BS09-0006). We thank the ESRF for providing access to beamtime and support through the Long Term Proposal MD830. The authors acknowledge H el ene Follet (Lyon, Lyon), R emy Gauthier (Turin, Italy) and David Mitton for sample preparation. The experiments reported here also feature in the PhD thesis of Boliang Yu (<https://tel.archives-ouvertes.fr/tel-02191449/document>).

Author contributions

F.P. designed the study. All authors participated to data acquisition. B.Y., C.O. and A.P. performed image reconstruction. B.Y. and F.P. did data analysis and B.Y. and C.O. performed statistical analysis. B.Y., P.C., A.P. and F.P. wrote the manuscript and all authors corrected the manuscript.

Competing interests

The authors declare no competing interests.

Additional information

Supplementary information is available for this paper at <https://doi.org/10.1038/s41598-020-61269-8>.

Correspondence and requests for materials should be addressed to F.P.

Reprints and permissions information is available at www.nature.com/reprints.

Publisher's note Springer Nature remains neutral with regard to jurisdictional claims in published maps and institutional affiliations.



Open Access This article is licensed under a Creative Commons Attribution 4.0 International License, which permits use, sharing, adaptation, distribution and reproduction in any medium or format, as long as you give appropriate credit to the original author(s) and the source, provide a link to the Creative Commons license, and indicate if changes were made. The images or other third party material in this article are included in the article's Creative Commons license, unless indicated otherwise in a credit line to the material. If material is not included in the article's Creative Commons license and your intended use is not permitted by statutory regulation or exceeds the permitted use, you will need to obtain permission directly from the copyright holder. To view a copy of this license, visit <http://creativecommons.org/licenses/by/4.0/>.

  The Author(s) 2020